Flow Measurement and Instrumentation 83 (2022) 102122

Contents lists available at ScienceDirect

Flow Measurement and Instrumentation

journal homepage: www.elsevier.com/locate/flowmeasinst

On air entrapment onset and surface velocity in high-speed turbulent prototype flows

Hubert Chanson

The University of Queensland, School of Civil Engineering, Brisbane, QLD, 4072, Australia

ARTICLE INFO

Keywords:
Free-surface flows
Air entrapment onset
Full-scale prototype spillway
High speed
Strong turbulence
Optical technique

ABSTRACT

In a free-surface spillway, the upstream flow is non-aerated and the flow becomes a strong air-water mix downstream of the onset location of air entrapment. Field observations were conducted over a steep spillway chute, and detailed quantitative measurements were undertaken in real-world high-speed flows with strong turbulence and very high Reynolds numbers within the range 10^7 to 10^8. The data showed that the onset of air entrapment is a complicated transient three-dimensional process in high-speed strongly-turbulent flows. A robust optical flow (OF) technique was applied and provided physically-meaningful surface velocities in the non-aerated flow region. The streamwise velocities were reasonably close to ideal fluid flow calculations, with large streamwise surface velocity fluctuations, in the non-aerated flow region. Overall, the study demonstrated the application of optical techniques to prototype spillway flows, provided that some careful validation was undertaken.

1. Introduction

In high-velocity open channel flows, free-surface aeration is commonly observed (Fig. 1) and called 'white waters' [1]. At an un-gated spillway crest, the flow changes from a subcritical motion in the reservoir to a torrential motion on the chute in a relatively smooth manner, as the flow is accelerated [2]. On the chute, a turbulent boundary layer develops at the upstream end [3]. The onset of free-surface aeration is typically observed when the outer edge of the boundary layer generates turbulent shear stresses, acting next to the free-surface, large enough to break the water surface [4,5]. Downstream, i.e. in the air-water flow region, the instantaneous separation between the water and atmosphere exhibits a complicated structure, with two interpenetrating and interacting phases [6,7]. Fig. 1 illustrates the high-speed flow down two large prototype chutes: the 335 m wide Paradise dam spillway (Fig. 1A) and the 12.25 m wide Hinze dam spillway (Fig. 1B & C). In each photograph, the upstream non-aerated region, the inception region of free-surface aeration, and the aerated 'white water' region are clearly seen. The figure caption provides details of each flow condition.

In the present study, some field observations on a large prototype chute are presented and analysed, and the results are discussed. A novel feature of the study is the detailed quantitative measurements in a real-world fluid flow, with high-speed, strong turbulence, and very-high Reynolds numbers within the range 10^7 to 10^8. The role of streamwise flow structures is discussed in the non-aerated flow region, leading to the formation of elongated air-water surface structures in the onset region. The results show that the onset of air entrapment is complicated and three-dimensional, with transient localised two-phase interactions.

2. Investigation site, methodology and approach

The investigation was undertaken at the Hinze dam, in eastern Australia, between March 2013 and March 2021 (Fig. 1B & C). The dam is equipped with a steep spillway chute, discharging into a stilling basin located about 35 m below the crest. The spillway crest had a round ogee profile leading to a stepped chute. The chute slope was 1 V:0.9H ($\theta = 51.3°$) and the step height was 1.5 m (h = 1.5 m). Visual, photographic and cinematographic observations were conducted from two sturdy concrete platforms, one located downstream of and facing the spillway chute, and another immediately above the spillway crest centreline. Fig. 1B and C shows hand-held photographs taken from each platform respectively. The observations were performed with three dSLR cameras (sensor resolutions between 12 Mpx and 24 Mpx), equipped with prime lenses producing photographs and movies with negligible barrel distortion. Movies were recorded in high definition (1920 × 1080 px) at

Abbreviations: IRQIV, Infrared Quantitative Image Velocimetry; LSPIV, Large Scale Particle Image Velocimetry; OF, Optical Flow; px, pixel.

E-mail address: h.chanson@uq.edu.au.

https://doi.org/10.1016/j.flowmeasinst.2022.102122
Received 26 July 2021; Received in revised form 14 September 2021; Accepted 4 January 2022
Available online 6 January 2022
0955-5986/

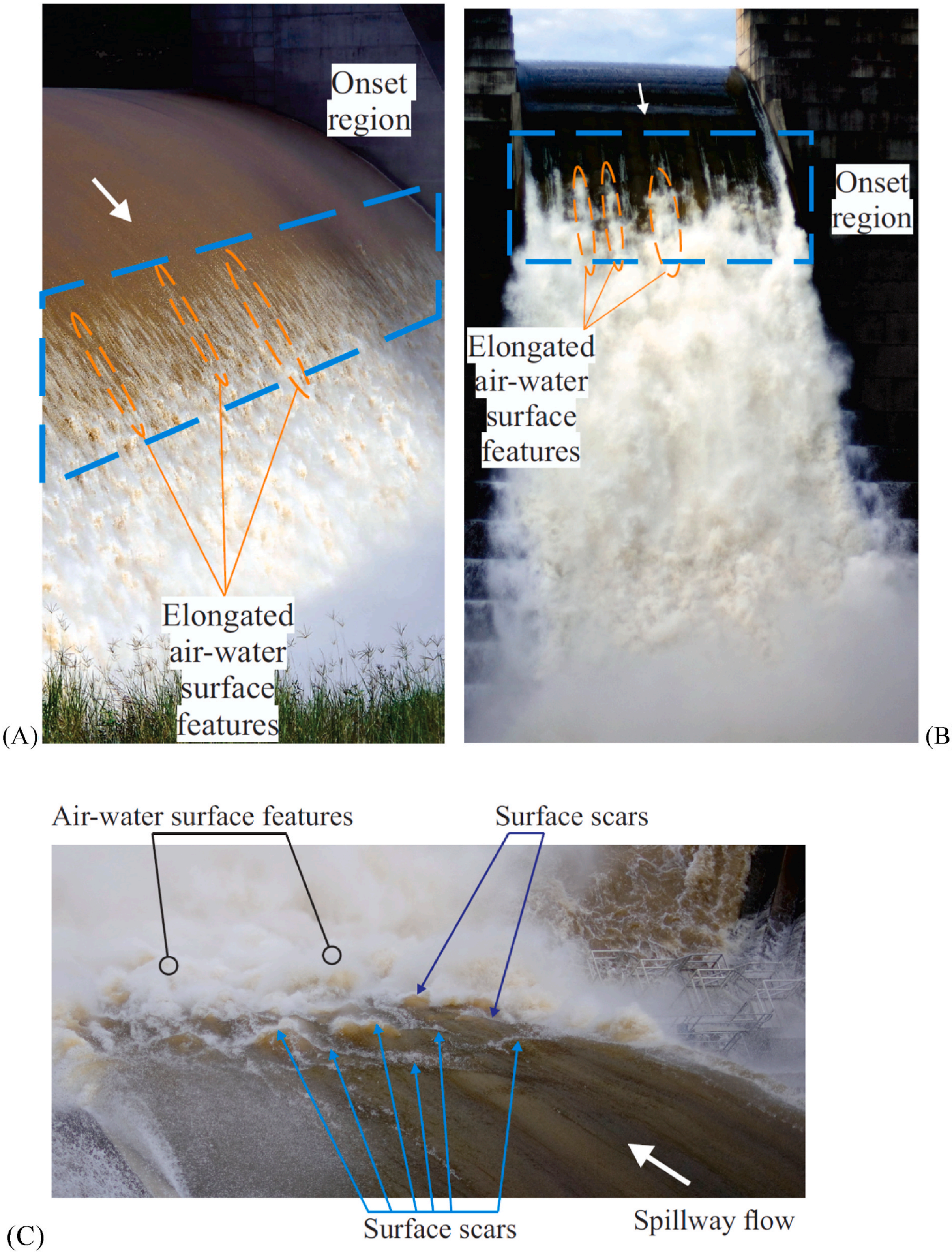

Fig. 1. Prototype spillway chutes in operation - (A) Paradise dam on March 5, 2013: $Q = 2320$ m^3/s, $Re = 7.3 \times 10^6$, $\theta = 57.4°$, steps: $h = 0.62$ m, $q^{2/3}/(g^{1/3} \times h) = 2.8$, shutter speed: 1/1600 s; (B) Hinze dam on March 27, 2021, $Q = 72$ m^3/s, $Re = 2.3 \times 10^7$, $\theta = 51.3°$, steps: $h = 1.5$ m, $q^{2/3}/(g^{1/3} \times h) = 1.0$, shutter speed: 1/8000 s; (C) Hinze dam on January 29, 2013, $Q = 202$ m^3/s, $Re = 6.5 \times 10^7$, $\theta = 51.3°$, steps: $h = 1.5$ m, $q^{2/3}/(g^{1/3} \times h) = 2.02$, shutter speed: 1/8000 s, view from upstream.

30 fps and 60 fps. The water discharge was deduced from the measured reservoir elevation, using the predicted discharge coefficient and checked against the rating curve [8].

The field measurements were performed with water discharges within 71 m^3/s $< Q <$ 334 m^3/s, and bulk Reynolds number between $2.3 \times 10^7 < Re < 1.08 \times 10^8$. For these flow conditions, the water was skimming above the pseudo-invert formed by the step edges, since the dimensionless discharges satisfied: $q^{2/3}/(g^{1/3} \times h) > 0.9$, q being the discharge per unit width and g the gravity acceleration.

The analyses of surface scars at the downstream end of the clear-water region were conducted in terms of their transverse characteristics, based upon video movies taken from above the spillway crest. The surface features in the onset region were analysed based upon both high-shutter speed photographs and video-movies. While the use of high-shutter speed photographs reduced the amount of available data, the high resolution enabled a fine geometrical characterisation. In all the cases, the analyses, tracking and measurements of the air-water surface characteristics were conducted manually to guarantee the best quality control, owing to the complexity of the prototype turbulent flow motion, associated with very rapid, unpredictable changes in space and time.

A number of movies taken from the downstream platform were analysed using an optical flow (OF) technique, with the camera fixed on a tripod. The Optical Flow (OF) is a set of tools, detecting the flow motion between consecutive frames based upon brightness intensity changes, originally developed by computer vision scientists (Appendix I). Although the brightness equations are not directly derived from the fluid mechanics principles, the OF technique may be applied to fluid flows [9,10]. Herein, the OF technique proposed by Farneback [11] was used to compute the instantaneous surface velocity field. The Farneback technique was applied using parameters previously obtained and validated in laboratory for surface velocity field (Appendix I). No attempt was made to "calibrate" the OF calculations, because of the number of intrinsic difficulties with field observations during flood events, including un-controlled flow and optical conditions [12]. With the camera field of view perpendicular to the spillway chute, the raw data included the vertical and horizontal transverse surface velocity components recorded at a vertical elevation. The streamwise surface velocity was deduced from the vertical surface velocity component and invert profile based upon continuity, energy and geometric considerations, assuming a two-dimensional flow [12].

3. High-speed flow patterns

For all discharges, the stepped chute flow presented a free-surface appearance similar to that of smooth chute flows. The water discharge skimmed on the pseudo-bottom formed by the step edges. The upstream flow was un-aerated, exhibiting a darker brown colour because of suspended matters (Fig. 1). The inception of air entrapment was clearly marked and the free-surface become white downstream of the onset region.

Downstream of the spillway crest, the non-aerated flow free-surface presented some surface undulations, best seen in the sun glare, e.g. on 24 and March 27, 2021. Further, some network of longitudinal surface ridges were seen developing upstream of the spillway crest and persisting up to the inception region. In the vicinity of and immediately upstream of the onset region, large-scale turbulent structures were seen to interfere with the free-surface, in the form of large well-defined surface scars and boils (Figs. 1C & 2). The dynamics of surface scars highlighted the interaction of tilted quasi-streamwise tubular vortices with the water surface, visualised computationally by Toro et al. [13] and Zabaleta and Bombardelli [14]. The strong interfacial turbulence induced by these interactions led to some transient two-phase air-water free-surface motion, with air-water packets exploding through the water surface. On several occasions, i.e. in 2013 and 2021, the interactions of these large vortices with the free-surface generated "eruptions" of air-water entities surging 200–400 mm above the mean free-surface, with extreme events reaching over 800–1000 mm above the free-surface, i.e. in the direction perpendicular to the water surface. These powerful eruptions of air-water masses were believed to be energetic collisions of tilted large-scale powerful streamwise vortices with the upper surface, in the onset region. The exact location of air entrapment onset was constantly changing and fluctuating about a mean position. At a given instant, the "onset location" was not a straight transverse line, but more a surface plane with a transient "zebra" pattern, observed at both Paradise and Hinze dam spillways (Fig. 1), as well as other dam spillways. High-shutter speed photographs showed the presence of short-lived elongated air-water surface structures, somehow similar to those observed by Arosquipa Nina et al. [15] in a large-size stepped spillway model. Downstream of the onset region, the free-surface was white, with some emulsions of air and water and a complicated structure of the air-water continuum [6,7] (Fig. 1).

In the high-velocity chute flows, some short-lived energetic surface scars were observed immediately upstream of the onset region (Figs. 1C & 2) [16]. The surface scars were analysed in terms of their transverse characteristics at the downstream end of the non-aerated region. A detailed statistical summary is presented in Appendix II and typical data are reported in Fig. 3. Visually, the surface scars initiated and developed primarily as transverse entities, although the generation process could include a mix of both longitudinal and transverse scar initiation. The initial scar development was followed by an upward growth induced by some violent upwelling, leading to breaking and air-water mixing (Fig. 1C). The observations across several flood events suggested some common pattern of interactions between large vortices and free-surface, associated with some pseudo-hairpin vortex head interacting with the free surface, in turn inducing a strong deformation and ultimately some breaking of the water surface. The onset of free-surface aeration tended to follow a scheme, sketched in Fig. 2. Large bottom-induced vortices structures approached the free-surface and deformed the water surface. The very-large-scale coherent structures were shed into the outer flow, and attached to the free-surface when they encountered the interface,

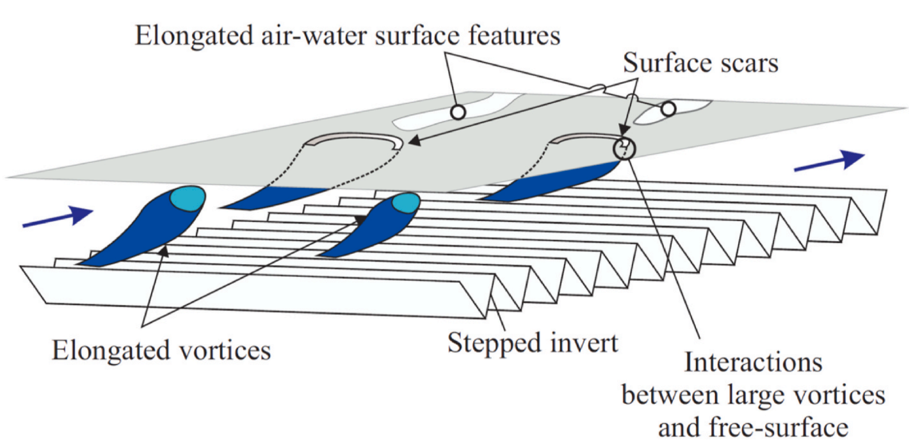

Fig. 2. Three-dimensional sketch of elongated vortical structures interacting with free-surface in the onset region in a prototype stepped chute - Tilted schematic with overflow direction from left to right.

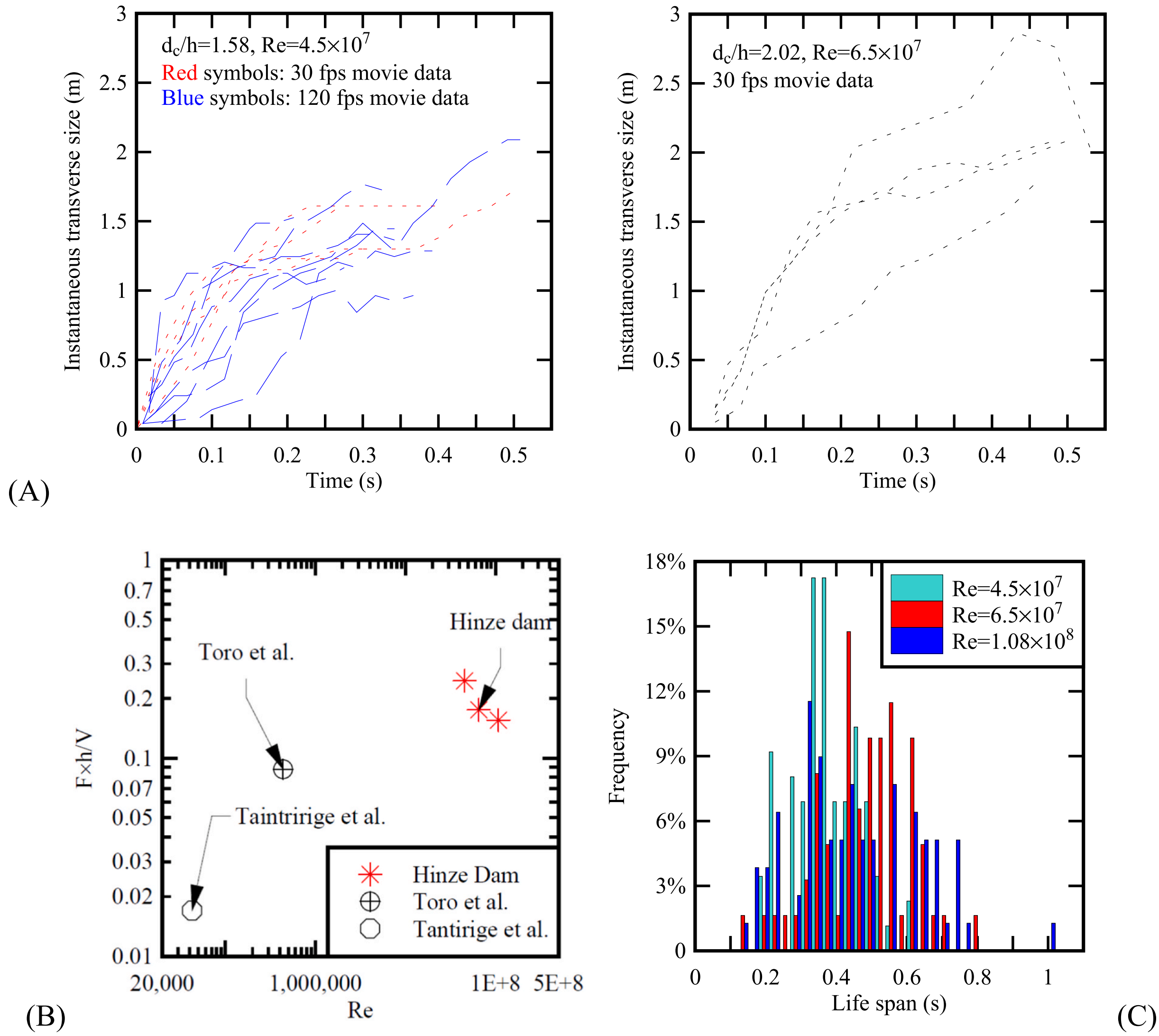

Fig. 3. Characteristics of individual surface scars immediately upstream of the inception region of free-surface aeration - (A) Transverse growth of individual surface scars on March 24, 2021 (Left) and January 29, 2013 (Right); (B) Dimensionless frequency of surface scar generation rate fluctuation immediately upstream of the inception region: comparison with cavity ejection frequency with triangular cavities [13,17]; (C) Distributions of surface scar lifespan between first appearance and disappearance.

Date	Q (m^3/s)	q (m^2/s)	$q^{2/3}/(g^{1/3} \times h)$	Re
24/3/2021	140	11.4	1.58	4.5×10^7
29/1/2013	202	16.5	2.02	6.5×10^7
24/3/2021	140	11.4	1.58	5.1×10^7

generating a mostly-transverse scar. This was followed by some violent upwelling, often characterised by a very-rapid growth of the scar. Some upward stretching of the scar occurred, with intense breaking, air and water expulsion, as well as air entrapment (Fig. 1C). The surface breaking led to the formation of elongated air-water surface ribbons, seen in Fig. 1A and B, before the complete aeration of the whole free-surface, i.e. the air-water flow region downstream of the onset region. Altogether, the onset of air entrapment was a highly transient process, starting with the generation of surface scars and followed by some violent upwelling and breaking, combined with energetic explosions and implosions of the water surface, that could not be contained by surface tension.

The visual observations showed a large generation rate of surface scars. Herein, a scar generation was defined as the onset of the scar development: i.e., the smallest surface disturbance at the initiation of the scar. The average generation rate per unit width was about 1.4 Hz/m to 2.2 Hz/m (Appendix II). The temporal development of individual scars suggested an initially slow growth immediately after onset, followed by a very rapid transverse growth, with instantaneous transverse growth rates in excess of 10 m/s and up to 25 m/s, lasting 0.015 s–0.025 s, and continuing at a slower transverse growth combined with an upward deformation of the scar structure, until scar collapse, explosion, implosion, merger or disappearance. The temporal change in growth rate was observed both qualitatively and quantitatively in all data sets (Fig. 3A). Typical individual scar growth observations are presented in Fig. 3A. The data further showed some periodicity of scar appearance (i.e. generation rate) at the water surface, with mean periods between 0.43 s and 0.47 s. The frequencies in scar generation rate fluctuations are reported in a dimensionless form in Fig. 3B, using the water depth and surface velocity in the onset region as relevant length and velocity scales respectively. In Fig. 3B, the present spillway data are compared to the characteristic cavity ejection frequency for triangular cavities, i.e. laboratory data [17] and CFD computations [13]. The data showed a monotonic increase in dimensionless frequency with increasing Reynolds numbers, hinting that the fluctuations in surface scar generation rate could be linked to some large-scale-vortex shedding induced by the succession of step edges (Fig. 2) and the irregular sequential triangular cavity ejections.

The whole growth of a sizeable number of individual scars was documented from onset to disappearance. Typical results are presented in Fig. 3C and a statistical summary is detailed in Appendix II. The present data applied to individual structures, and larger scar structures, observed when several surface scars merged, were not accounted for. The average lifespan of individual scars ranged from 0.37 s to 0.47 s (Fig. 3C). Their final transverse size was between 1.2 m and 1.5 m in average, with an average final size increasing with increasing Reynolds number (Appendix II). The average scar growth rate was about 3 m/s to 4 m/s, between inception to disappearance, although much larger instantaneous transverse growth rates were seen during the rapid growth sequence.

4. Surface velocity

The Optical Flow (OF) results focused on the streamwise surface velocity, measured tangential to the free-surface, and the spanwise surface velocity. First, the centreline OF surface velocity data were compared to the ideal fluid flow theory. The results showed a relatively close agreement between the streamwise OF surface velocity and the ideal fluid flow velocity upstream of the onset region, both qualitatively and quantitatively. Fig. 4A presents a typical comparison in terms of streamwise surface velocity component V_s, with the centreline streamwise surface velocity standard deviation v_s' and transverse surface velocity standard deviation v_t' added for completeness, together with the ideal fluid flow calculations (thick dashed line). In Fig. 4, the vertical axis is the vertical elevation, while the streamwise velocity component is positive downstream. Second, the OF data yielded very poor outputs in the air-water flow region downstream of the onset region (Fig. 4A).

A systematic comparison between OF and ideal fluid flow velocity showed a number of salient features. The streamwise surface velocity data showed a relatively close agreement with the ideal fluid flow velocity in the non-aerated flow region. That is, the surface velocity increased with decreasing vertical elevation, as ideally predicted. Practically, however, the quality of the OF data, hence the quality of the comparison, was closely linked to the quality of the original movies, including (a) the camera position ideally placed perpendicularly to the spillway chute, (b) the camera system equipment, i.e. camera body and lenses, preferably with professional-grade prime lenses, (c) the movie definition, with improved outputs with higher resolutions, (d) the lighting conditions, e.g. with best quality outputs in daylight sunny conditions and poor outcomes in low-light conditions and under heavy rainfall, and (e) the photographer's experience which improved between 2013 and 2021.

The OF surface velocity field was analysed in the non-aerated flow region. A typical data set is shown in Fig. 4. The figure caption provides the details of the overflow conditions. In each graph, the vertical axis is the vertical elevation z, the horizontal axis is the spanwise coordinate measured from the right training wall, and the legend corresponds to the OF data. The mean location of the onset region of free-surface aeration is shown as a thick solid line. Upstream of the onset region, the surface velocity map showed the acceleration of the flow, with a trend consistent with the ideal fluid flow theory (Fig. 4A). The data showed large standard deviations of the streamwise surface velocity v_s', likely caused by a combination of "true" surface velocity turbulence and relatively large velocity fluctuations initiated by water surface fluctuations (Fig. 4A). The latter was previously reported in laboratory [18–20] and might be caused by a combination of upstream flow disturbances, some longitudinal undular pattern induced by the stepped invert profile, and the free-surface interaction with the large-scale vortical structures shed at each step (e.g. Fig. 2). In contrast, the spanwise surface velocity fluctuations v_t' were much smaller (Fig. 4A). The ratio of spanwise surface velocity fluctuations to streamwise surface velocity was v_t'/V_s ~0.05 to 0.1, comparable to rough turbulent boundary layer data [21, 22].

The OF surface velocity maps further suggested the presence of longitudinal "streets" of lower surface velocities, with streaks of faster flowing fluid in between, near the inception region (Fig. 4B). While the position of these surface currents varied with time, their lateral spacing tended to be well-defined and consistent with the high-shutter photographic observations of elongated air-water surface features (Fig. 1B).

Finally, the present OF technique gave physically meaningless data in the air-water flow region downstream of the inception region (Fig. 4A).

5. Discussion

While OF techniques have been previously applied to laboratory spillway chutes, any comparison between laboratory and prototype measurements is difficult, in part because of the inability to deploy the same type of hardware in a similar fashion with the harsh field conditions. During a natural disaster and major flood event, most field observations rely upon "general consumer" camera equipment, typically operating at 25 fps to 60 fps. While a higher frame rate would be highly desirable [12], it is not currently achievable. Although most laboratory data sets were based upon much higher camera frame rates, i.e. 1000 fps to 22,000 fps, the present camera setup yielded a drastically lesser temporal and spatial resolution, with a much lower frame rate (30–60 fps) and a lesser pixel per metre resolution, than in laboratory. Several OF parameters may further affect the velocity results [10,23], but their selection was less critical, in the author's experience, because of the relatively coarse spatial and temporal resolution in the prototype. Practically, the successful implementation of the OF to field observations relied more on the optical quality of the camera system (i.e. dSLR camera and prime lenses herein), stability of the camera support system (i.e. tripod installed on a concrete platform herein) and accuracy of the georeferencing, including ground control points (i.e. Hinze dam spillway drawings as built herein).

The present field observations may potentially lead to a different modelling approach, based upon some hybrid technique combining laboratory experiments and field observations, based upon some complementary observations that are geometrically-scaled based upon a Froude similarity. Fig. 5 documents a comparison in terms of the streamwise surface velocity in the non-aerated flow region between prototype and physical model data of stepped chutes. The data are presented in a dimensionless form based upon a Froude similarity, with H the total head, d_c the critical depth: $d_c = (q^2/g)^{1/3}$ and V_c the critical velocity: $V_c = (g \times q)^{2/3}$. The results showed a good agreement between prototype data (thick lines), laboratory data (cross symbols) and ideal fluid flow calculations (tick red dashed line) in the developing non-aerated flow region (Fig. 5). In practice, a larger scatter was seen with the field observations compared to laboratory data, owing to the intrinsic difficulties of any field deployment.

Generally, the use of optical techniques during high-speed prototype operations remains challenging and it is still in infancy. There is no doubt that Large-Scale Particle Image Velocimetry (LSPIV), Infrared Quantitative Image Velocimetry (IR-QIV) and OF techniques may deliver some important details on the velocity field [12,25–27], possibly complemented by marine radar techniques [28]. Yet, all the optical techniques require some systematic and independent validation. This is not simple and a careful validation is very challenging. The few relevant studies showed a number of non-trivial issues (e.g. Ref. [29]. Any imaging technique relies upon adequate recording position(s) with good illumination and minimum shadows and glare. The water surface must

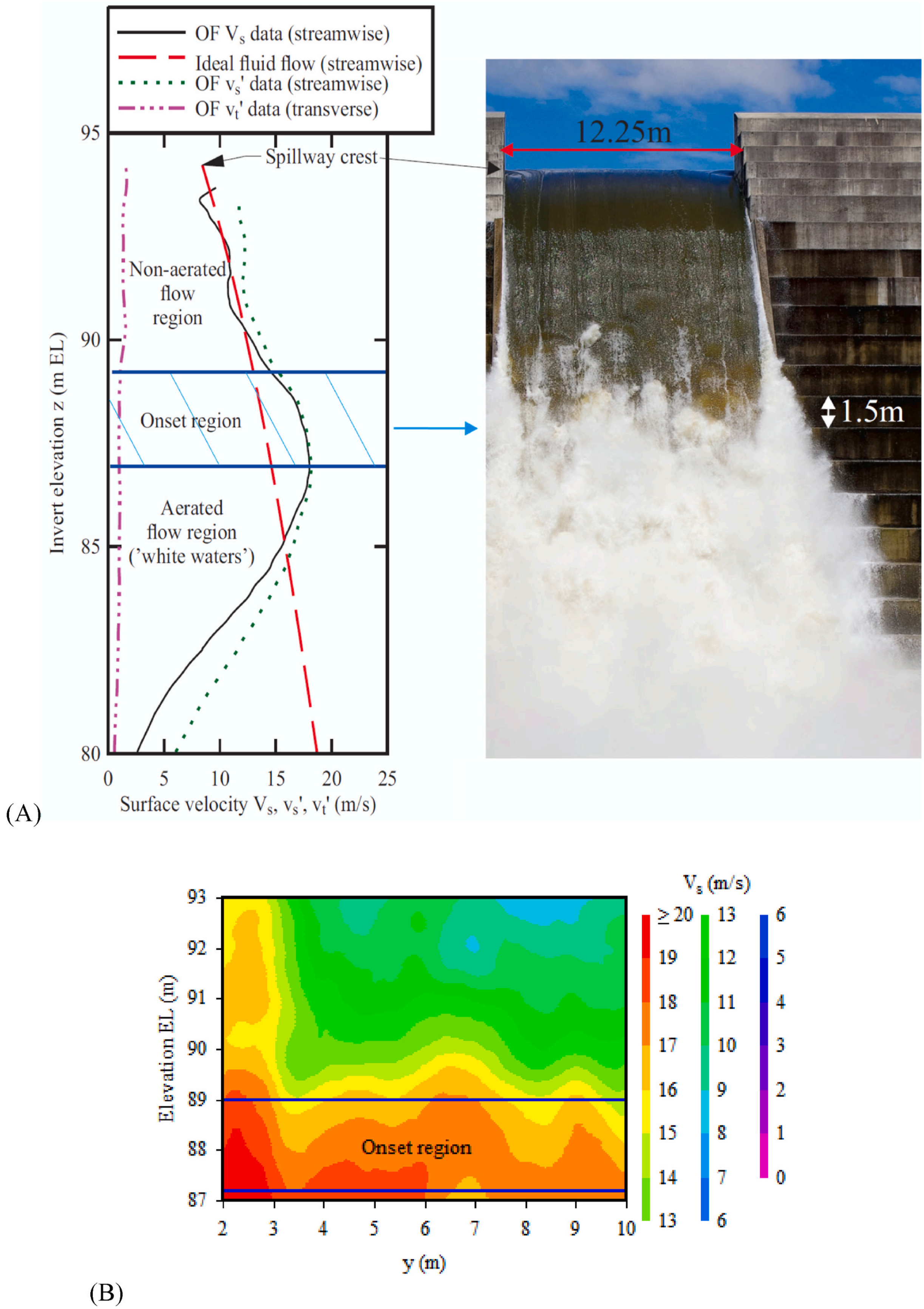

Fig. 4. OF surface velocity on the Hinze dam spillway for Q = 150 m^3/s, Re = 4.54×10^7, $\theta = 51.3°$, steps: h = 1.5 m, $q^{2/3}/(g^{1/3} \times h) = 1.58$, Number of analysed frames: 4000 - (A) Comparison between centreline OF velocity and ideal fluid flow velocity (Left), with photograph of spillway chute flow corresponding to the data (Right); (B) Time-averaged streamwise surface velocity V_s map in the non-aerated region.

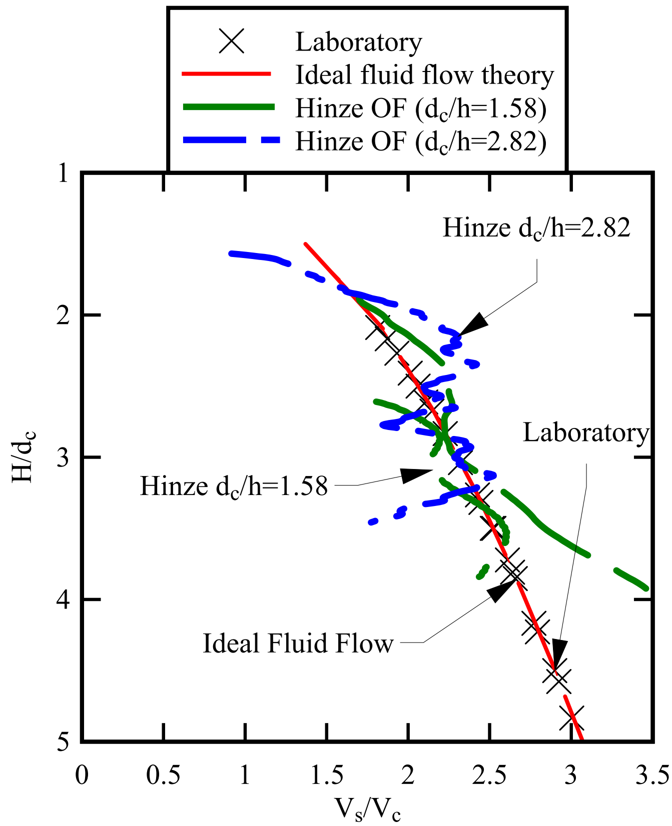

Fig. 5. Dimensionless comparison of streamwise surface velocity on the chute centreline in the non-aerated flow region between Prandtl-Pitot tube laboratory data, field OF observations and ideal fluid flow theory (Laboratory data [24]: - Ideal fluid calculations assuming hydrostatic pressure distributions.

Data	θ (°)	h (m)	$q^{2/3}/(g^{1/3} \times h)$	Re	Instrumentation	Reference
Laboratory	45.0	0.10	0.9 to 1.7	1.1×10^6 to 4.4×10^6	Prandtl-Pitot tube	Zhang and Chanson [24]
Hinze dam	51.3	1.5	1.58	4.5×10^7	OF	Present study
			2.82	1.08×10^8		

provide some tracers. While seeding might be considered in subcritical fluvial regime, it is un-practical in high-velocity flows. With high-speed flows, some high-resolution high-speed camera equipment constitutes a further requirement, combined with some experienced operator. As with any field work undertaken during major floods and potentially natural disasters, the physical access may be a major challenge, when the access roads are under water, not to mention the optical access to the high-speed flow.

6. Conclusion

In a prototype chute, the onset of air entrapment in high-speed strongly-turbulent flow is complex, transient and three-dimensional. The free-surface immediately upstream of the aerated flow region presents some highly unsteady surface scars, contributing to rapid air entrapment with the formation of elongated surface features. A robust optical flow (OF) technique was applied to video movies taken from a tripod installed on a very-sturdy downstream platform. The OF data delivered physically meaningful surface velocities in the non-aerated flow region upstream of the onset region of air entrapment, with streamwise velocities reasonably close to ideal fluid flow calculations. Large streamwise surface velocity fluctuations were observed in the non-aerated flow region, while the spanwise surface velocity fluctuations were much smaller and close to rough boundary layer data.

Overall, the study demonstrated the application of optical technique in prototype spillway flows, provided that some careful solid validation is performed. The current study details the first successful detailed characterisation of air entrapment onset in a prototype chute operating across a range of large Reynolds numbers. Further, it paves the way for a different hybrid modelling technique blending field observations and geometrically-scaled laboratory experiments based upon a Froude similitude.

Author statement

Hubert Chanson: Conceptualization, Methodology, Software, Validation, Formal analysis, Investigation, Field measurements, Data Curation, Resources, Writing - Original Draft, Writing - Review & Editing, Visualization, Project administration, Funding acquisition.

Declaration of competing interest

The authors declare the following financial interests/personal relationships which may be considered as potential competing interests: In line with recommendations of the Office of the Commonwealth Ombudsman (Australia) and international Committee on Publication Ethics (COPE), Hubert Chanson declares a major conflict of interest with Matthias Kramer, University of New South Wales Canberra (Australia).

Acknowledgments

The author acknowledges Mr Barton Maher (Seqwater) for providing technical details of the Hinze dam spillway, as well as all the Seqwater personnel who assisted the author during technical visits. He also thanks Mr Rui (Ray) Shi (The University of Queensland) for his technical advice on the optical flow calculations. He further acknowledges some helpful and insightful inputs from Dr Gangfu Zhang (AECOM, Australia) and Dr John Macintosh (Water Solutions, Australia). The associate editor and reviewers are thanked for their constructive comments. The financial support of the University of Queensland, School of Civil Engineering is acknowledged.

In line with recommendations of the International Committee on Publication Ethics (COPE) and the Office of the Commonwealth Ombudsman (Australia), Hubert Chanson declares a major conflict of interest with Matthias Kramer (UNSW, Canberra).

Appendix I - On optical flow analysis

The Optical Flow (OF) is the apparent motion field between two consecutive images based upon the brightness change, and the true physical meaning depends on the projective nature of the items in motion [9,30]. The technique has been recently applied to fluid mechanics problems, with a focus on side views of sediment-laden jets and self-aerated chute flows [10,23,31].

A number of OF techniques have been used in fluid mechanics. The traditional Horn-Schunck technique [32] was applied by Refs. [10,31]; combined with image-pyramid application to handle large displacements [23]. applied both the Lucas-Kanade technique [33] and Farneback technique [11], and they showed more reliable results with the Farneback method. The robustness of the Farneback technique was further verified by Ref. [34] across different air-water turbulent shear flows, including a stationary hydraulic jump, a plunging air-water jet and a highly unsteady breaking bore. In the present study, the Farneback technique was adopted for the post processing of the data, following its application to surface velocity field by Ref. [15].

Appendix II - Statistical summary of surface scars characteristics immediately upstream of the inception of free-surface aeration

	Date:	Jan. 29, 2013	Mar. 31, 2017	Mar. 24, 2021
Parameter	Units			
$Q =$	m^3/s	202	334	140
$q^{2/3}/(g^{1/3} \times h) =$	–	2.02	2.82	1.58
Re =	–	6.5×10^7	10.8×10^7	4.54×10^7
Nb of scar generation observations:	–	341	415	259
Average production rate of surface scars per unit width:	(Hz/m)	1.93	2.20	1.44
Characteristic frequency F_{scar} in scar production rate fluctuations	(Hz)	2.11	2.34	2.29
$F_{scar} \times h/V_I =$	–	0.18	0.16	0.25
$F_{scar} \times d_I/V_I =$	–	0.21	0.13	0.22
Nb of detailed observations of scars:	–	96	78	87
Scar lifespan				
Average lifespan	(s)	0.47	0.44	0.37
Median lifespan	(s)	0.50	0.43	0.37
Standard deviation lifespan	(s)	0.13	0.18	0.10
Skewness lifespan		−0.30	+0.46	+0.29
Scar (final) transverse size				
Average transverse size	(m)	1.29	1.48	1.23
Median transverse size	(m)	1.30	1.40	1.19
Standard deviation transverse size	(m)	0.31	0.38	0.26
Skewness transverse size			0.11	+0.13
Scar (mean) growth rate				
Average growth rate	(m/s)		2.85	3.48
Median growth rate	(m/s)		2.87	3.28
Standard deviation growth rate	(m/s)		0.73	0.97
Skewness growth rate			0.36	+1.09

Notes: Characteristics of individual surface scars, prior to merging, collapsing or exploding; d_I: flow depth at inception of free-surface aeration: V_I: flow velocity at inception of free-surface aeration.

References

[1] N.S.L. Rao, H.E. Kobus, Characteristics of self-aerated free-surface flows, Water and Waste Water/Current Research and Practice, vol. 10, Eric Schmidt Verlag, Berlin, Germany, 1974.
[2] F.M. Henderson, Open Channel Flow, MacMillan Company, New York, USA, 1966.
[3] I.R. Wood, P. Ackers, J. Loveless, General method for critical point on spillways, J. Hydraul. Eng. ASCE 109 (2) (1983) 308–312.
[4] I.R. Wood, Air Water Flows, Proc. 21st IAHR Congress, Melbourne, Australia, Keynote address, 1985, pp. 18–29.
[5] I.R. Wood, Air entrainment in free-surface flows, in: *IAHR Hydraulic Structures Design Manual No. 4*, Hydraulic Design Considerations, Balkema Publ., Rotterdam, The Netherlands, 1991, p. 149.
[6] H. Chanson, Air Bubble Entrainment in Free-Surface Turbulent Shear Flows, Academic Press, London, UK, 1997, p. 401.
[7] M. Brocchini, D.H. Peregrine, The dynamics of strong turbulence at free surfaces. Part 2. Free-surface boundary conditions, J. Fluid Mech. 449 (2001) 255–290.
[8] Hinze Dam Stage 3, Spillway design hydraulics, in: Hinze Dam Stage 3 Upgrade Detailed Design Report, Appendix 4C, 2012, p. 10. February.
[9] T. Liu, A. Merat, M.H.M. Makhmalbaf, C. Fajardo, P. Merati, Comparison between optical flow and cross-correlation methods for extraction of velocity fields from particle images, Exp. Fluid 56 (8) (2015) 1–23.
[10] D.B. Bung, D. Valero, Optical flow estimation in aerated flows, J. Hydraul. Res. IAHR 54 (5) (2016) 575–580, https://doi.org/10.1080/00221686.2016.1173600.
[11] G. Farneback, Two-frame motion estimation based on polynomial expansion, in: Proc. Scandinavian Conference on Image Analysis, Springer, Berlin, Heidelberg, 2003, pp. 363–370.
[12] H. Chanson, Stepped spillway prototype operation, spillway flow and air entrainment: the Hinze dam, Australia, in: Hydraulic Model Report No. CH123/21, School of Civil Engineering, The University of Queensland, Brisbane, Australia, 2021, p. 183, https://doi.org/10.14264/c8d5280.
[13] J.P. Toro, F.A. Bombardelli, J. Paik, Detached eddy simulation of the nonaerated skimming flow over a stepped spillway, J. Hydraul. Eng. ASCE 143 (No. 9) (2017) 14. Paper 04017032.
[14] F. Zabaleta, F.A. Bombardelli, Eddy-resolving simulation of flows over macro-roughness, in: Proceedings of RiverFlow2020, CRC Press, Uijttewaal, 2020, pp. 1293–1299.

[15] Y. Arosquipa Nina, R. Shi, D. Wüthrich, H. Chanson, Intrusive and non-intrusive air-water measurements on stepped spillways with inclined steps: a physical study on air entrainment and energy dissipation, in: Hydraulic Model Report No. CH121/21, School of Civil Engineering, The University of Queensland, Brisbane, Australia, 2021, p. 258, https://doi.org/10.14264/e3f4d48. & 8 video movies.
[16] H. Chanson, Interactions between a developing boundary layer and the free-surface on a stepped spillway: Hinze dam spillway operation in january 2013, in: Proc. 8th International Conference on Multiphase Flow ICMF 2013, 2013. Jeju, Korea, 26-31 May, Gallery Session ICMF2013-005 (Video duration: 2:15), https://espace.library.uq.edu.au/view/UQ:301643.
[17] S.C. Tantirige, A.P. Iribarne, M. Ojhas, O. Trass, The turbulent boundary layer over single V-shaped cavities, Int. J. Heat Mass Tran. 37 (1994) 2261–2271.
[18] D.B. Bung, Non-intrusive measuring of air-water flow properties in self-aerated stepped spillway flow, in: Proc. 34th IAHR World Congress, Brisbane, Australia, 26 June-1 July, Engineers Australia Publication, Eric Valentine, Colin Apelt, James Ball, Hubert Chanson, Ron Cox, Rob Ettema, George Kuczera, Martin Lambert, Bruce Melville and Jane Sargison Editors, 2011, pp. 2380–2387.
[19] S. Felder, H. Chanson, Air–water flows and free-surface profiles on a non-uniform stepped chute, J. Hydraul. Res. IAHR 52 (2) (2014) 253–263, https://doi.org/10.1080/00221686.2013.841780.
[20] D. Valero, H. Chanson, D.B. Bung, Robust estimators for free surface turbulence characterization: a stepped spillway application, Flow Meas. Instrum. 76 (2020) 12, https://doi.org/10.1016/j.flowmeasinst.2020.101809, paper 101809.
[21] H. Schlichting, Boundary Layer Theory, seventh ed., McGraw-Hill, New York, USA, 1979.
[22] M.F. Tachie, Open Channel Turbulent Boundary Layers and Wall Jets on Rough Surfaces, Ph.D. thesis, Dept. of Mech. Eng., University of Saskatchewan, Canada, 2001, p. 238.
[23] G. Zhang, H. Chanson, Application of local optical flow methods to high-velocity free-surface flows: validation and application to stepped chutes, Exp. Therm. Fluid Sci. 90 (2018) 186–199, https://doi.org/10.1016/j.expthermflusci.2017.09.010.
[24] G. Zhang, H. Chanson, Hydraulics of the developing flow region of stepped spillways. II: pressure and velocity fields, J. Hydraul. Eng. ASCE 142 (No. 7) (2016) 9, https://doi.org/10.1061/(ASCE)HY.1943-7900.0001136).
[25] R. Le Boursicaud, L. Penard, A. Hauet, F. Thollet, J. Le Coz, Gauging extreme floods on YouTube: application of LSPIV to home movies for the post-event determination of stream discharges, Hydrol. Process. 30 (2016) 90–105.
[26] J. Le Coz, B. Renard, V. Vansuyt, A. Hauet, M. Jodeau, Video-based hydrometry: a Bayesian camera calibration method for uncertainty analysis, in: Proceedings of RiverFlow2020, CRC Press, Uijttewaal, 2020, pp. 1053–1060.
[27] S.A. Schweitzer, E.A. Cowen, Instantaneous riverwide water surface velocity field measurements at centimeter scales using infrared quantitative image velocimetry, AGU, Water Resourc. Res. 57 (2021) 28, https://doi.org/10.1029/2020WR029279. Paper e2020WR029279.
[28] Y. Li, D.Z. Pan, H. Chanson, C.H. Pan, Real-time characteristics of tidal bore propagation in the qiantang river estuary, China, recorded by marine radar, Continent. Shelf Res. 180 (2019) 48–58, https://doi.org/10.1016/j.csr.2019.04.012.
[29] M. Muste, I. Fujita, A. Hauet, Large-scale particle image velocimetry for measurements in riverine environments, AGU, Water Resourc. Res. 44 (2008) 14, https://doi.org/10.1029/2008WR006950. Paper W00D19.
[30] J.L. Barron, D.J. Fleet, S.S. Beauchemin, Performance of optical flow techniques, Int. J. Comput. Vis. 12 (1) (1994) 43–77.
[31] T. Liu, L. Shen, Fluid flow and optical flow, J. Fluid Mech. 614 (2008) 253–291.
[32] B.K. Horn, B.G. Schunck, Determining optical flow, Artif. Intell. 17 (1–3) (1981) 185–203.
[33] B.D. Lucas, T. Kanade, An iterative image registration technique with an application to stereo vision, IJCAI 81 (No. 1) (1981) 674–679.
[34] R. Shi, D. Wüthrich, H. Chanson, Applications of optical flow technique in air-water flows, in: H. Chanson, R. Brown (Eds.), *Proceedings of 22nd Australasian Fluid Mechanics Conference AFMC2020*, Brisbane, Australia, 7-10 December, Published by the University of Queensland, 2020, p. 4, https://doi.org/10.14264/d44ca31. Paper 21.

Hubert Chanson is Professor of Civil Engineering at the University of Queensland, Australia, where he has been since 1990, having previously enjoyed an industrial career for six years. His main field of expertise is environmental fluid mechanics and hydraulic engineering, both in terms of theoretical fundamentals, physical and numerical modelling. He leads a group of 5–10 researchers, largely targeting flows around hydraulic structures, two-phase (gas-liquid and solid-liquid) free-surface flows, turbulence in steady and unsteady open channel flows, using computation, lab-scale experiments, field work and analysis. He has published over 1200 peer-reviewed publications including two dozen of books. He serves on the editorial boards of International Journal of Multiphase Flow, Flow Measurement and Instrumentation, and Environmental Fluid Mechanics, the latter of which he is currently a senior Editor. He chaired the Organisation of the 34th IAHR Word Congress and 22nd Australasian Fluid Mechanics Conference, held in Brisbane (Australia) in June 2011 and December 2020 respectively.